1 **The interaction between the SEIS seismometer of the InSight Martian**

2 **mission and a regolith simulant**

3 Pierre Delage[1], Juan-Pablo Castillo Betancourt[1,2], Bernardo Caicedo Hormaza[2], Foivos

4 Karakostas[3], Emmanuel De Laure[1], Philippe Lognonné[4], Daniele Antonangeli[5], Bruce

5 Banerdt[6]

6 [1] Ecole des Ponts ParisTech, Laboratoire Navier/CERMES, UMR CNRS 8205, France

7 [2] Universidad de Los Andes, Bogota, Colombia

8 [3] Istituto Nazionale di Geofisica e Vulcanologia, Bologna, Italia

9 [4] Université de Paris, Institut de Physique du Globe, UMR CNRS 7154, France

10 [5] Sorbonne Université, Institut de minéralogie, de physique des matériaux et de
11 cosmochimie, UMR CNRS 7590, France

12 [6] Jet Propulsion Laboratory, NASA – CalTech, Pasadena CA, USA

13 Delage: ORCID 0000-0002-2101-5522 – Castillo Betancourt: ORCID 0000-0003-3123-4654 –
14 Caicedo Hormaza: ORCID 0000-0003-4344-0914

15

16

17

19

1

20 **Abstract**

21 A detailed investigation of the interaction between a Martian regolith simulant and the foot

22 of a seismometer (SEIS) recently deployed on the surface of Mars within the NASA InSight

23 mission has been conducted. A specific device used to investigate the SEIS/ground

24 interaction was improved to provide accurate measurements of low forces and

25 displacements, with a higher system stiffness and appropriate thermal insulation. A series

26 of tests were carried out with a 60 mm diameter disk and the SEIS foot (disk with a spike in

27 the disk centre). The maximum disk penetration in the loose sand used as simulant under

28 the SEIS weight (10 N) was between 400 and 600 μm, with a tiny effect of the spike. Load

29 cycles under various forces were performed to investigate the elastic interaction, with good

30 reversibility and a linear change of the Young modulus with respect to the average vertical

31 stress. The tests provided comparable values, showing that the Young modulus was around

32 20 MPa, compatible with that of loose terrestrial sands and agreeing well with the seismic

33 wave velocities at surface (from laboratory experiments and from measuring on the surface

34 of Mars the travel times of waves received by the SEIS seismometer).

35

36 Keywords: Laboratory tests, sands, soil structure interaction

37

2

38　# 1. Introduction

39　The Seismic Experiment for Interior Structure (SEIS, Lognonné et al. 2019, 2020) of the NASA

40　(National Aeronautics and Space Administration) InSight mission on Mars (Interior

41　Exploration using Seismic Investigations, Geodesy and Heat Transport, Banerdt et al. 2020)

42　is the first seismometer ever deployed in direct contact with the surface of the planet Mars,

43　in the footsteps of the Apollo Lunar Surface Experiments Package on the Moon (e.g. Latham

44　et al. 1969, 1970; Bates et al. 1979) and 44 years after the landing of the two Viking

45　seismometers in 1976 (these seismometers, placed on the landers with no direct contact

46　with the ground, didn't provide any exploitable data). The InSight mission is a geophysical

47　mission aimed at further understanding the structure of Mars and of the other terrestrial

48　planets of the solar system. The main geophysical instruments deployed on Mars are a very

49　high sensitivity seismometer (SEIS) funded by the French space agency (CNES - Centre

50　National d'Etudes Spatiales) and the HP^3 instrument (Heat flow and Physical Properties

51　Package), a self-penetrating dynamic probe (called the mole, 39.6 cm long and 2.7 cm

52　diameter) funded by the German Institute for Planetary Research (DLR - Deutsches Zentrum

53　für Luft- und Raumfahrt). The HP^3 instrument is designed to perform thermal conductivity

54　measurements along the first $3 - 5$ meters below the surface. The InSight lander that landed

55　on Mars on 26 November 2018, is represented in the artist view of Figure 1, with both the

56　SEIS (covered by a wind and thermal shield) and the HP^3 instruments deployed. Both are

57　linked to the lander by tethers that transmit energy and data.

3
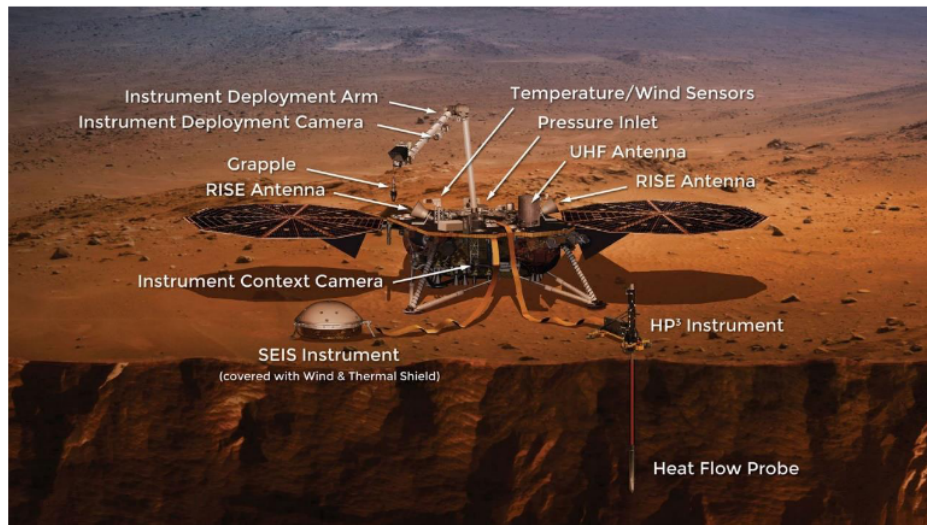
Figure 1. InSight NASA Lander concept and main instruments. Image Credit:
https://mars.nasa.gov/insight/spacecraft/instruments/summary/

61 The Figure also shows the 2 m long Instrument Deployment Arm (IDA) and its grapple that

62 deployed both SEIS and HP^3 on the ground. The IDA also carries a high-resolution

63 Instrument Deployment (colour) Camera (IDC). The lander is also equipped with an

64 Instrument Context Camera (ICC), a meteorological station including temperature,

65 windspeed and pressure sensors, two RISE antennas (Rotation and Interior Structure

66 Experiment) providing a precise location of the lander to accurately monitor the

67 movements of the planet from the Earth and an Ultra High Frequency antenna for data

68 transmission. Energy is provided by two twin 1.8 m diameter solar panels with a power of

69 700 W each, on clear days.

70 The average size of the regolith particles on Mars was determined from thermal inertia

71 measurements by the Viking lander and the Themis orbiter (Arvidson et al. 1989). The

72 microscopic imagers of the Mars Exploration Rovers (MER - Spirit and Opportunity, 2004),

73 Mars Science Laboratory (MSL - Curiosity, 2012) and Phoenix lander (2008) evidenced

4

74   sorted dark grey basaltic sub-rounded to rounded fine sand particles (due to wind saltation

75   under a 750 Pa atmospheric pressure), with diameter between 80 and 200 μm. This range

76   is compatible with the average diameter (170 μm) derived from thermal inertia measured

77   at the InSight landing site (160–230 J m^{-2} K^{-1} s$^{-1/2}$, Golombek et al., 2020). Bright red dust

78   particles (2 – 5 μm) of slightly chemically altered basalt are also observed (Arvidson et al.

79   2004a et b, Golombek et al. 2006a and b and Goetz et al. 2010). Orbiter observations

80   indicated that dust has been expelled by the rockets during landing at an average distance

81   of 20 m around the InSight lander (Golombek et al. 2020).

82   Figure 2 shows a high-definition IDC photo of the Martian surface in the InSight landing site,

83   showing the sand-like appearance of the regolith, with also some pebbles on the surface

84   around.

85
86   *Figure 2. IDC photo showing the scoop of the Instrument Deployment Arm compressing the regolith*
87   *above a hole developed around the self-penetrating mole during hammering. The scoop width is*
88   *7.6 cm (image credit NASA – CalTech).*

89   A detailed geological description of the so-called "Homestead hollow" where the lander is

90   located was presented by Golombek et al. (2020), from which the interpretative cross

5

91   section of the landing site of Figure 3 has been extracted. It shows a typical regolith profile,

92   with an around 3 m thick layer of relatively fine-grained impact generated regolith (3) that

93   likely grades with depth into coarse, blocky ejecta (2) that overlies fractured basalt flows

94   (1), with an estimated 10 m thick layer of blocky ejecta.
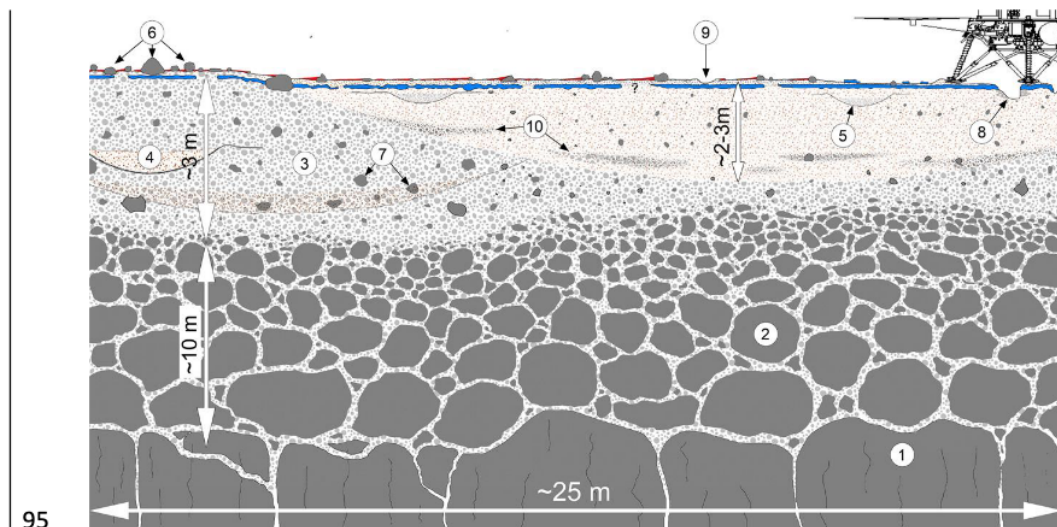
95
96   *Figure 3. Interpretative cross-section of the shallow surface beneath the InSight lander (Golombek*
97   *et al. 2020, Creative Commons CC BY license). 1: Fractured basalt flow; 2: Blocky ejecta; 3: Fine-*
98   *grained impact generated regolith; 4, 5: Overlapping craters; 6: Rockier area; 7: Rocks embedded*
99   *in regolith; 8: Pits opened by retro rockets during landing; 9: Surface divots; 10: Lens of ejecta from*
100 *other craters.*

101 This paper is devoted to further investigating the elastic interaction between the SEIS foot

102 and a Martian regolith simulant, by using a specific device working at very low stresses and

103 strains. In a first approach, the investigation was carried out under terrestrial gravity (9.81

104 m/s^2), higher than Mars' gravity (3.72 m/s^2). The aim of the program is to provide an

105 estimation of the value of the axial elastic spring constant of the regolith simulant to allow

106 for a theoretical modelling of the elastic interaction between the SEIS and the Martian

107 regolith (see Fayon et al. 2018). From a seismology point of view, the elastic parameters of

6

108   the surface regolith that can be derived from this experiment are also interesting to

109   estimate the wave velocity in the near surface.

110   2. Material and methods

111   2.1. Introduction

112   The shape of the SEIS foot, designed based on a first series of tests carried out in a device

113   developed at Ecole des Ponts ParisTech (Karakostas et al. 2013) is presented in Figure 4. The

114   foot consists of a disk with 60 mm diameter and a 20 mm long conic spike (10 mm diameter

115   at its base) in its centre. As further detailed in Section 2.3, the device was improved to get

116   a better accuracy in terms of displacement and force measurements.
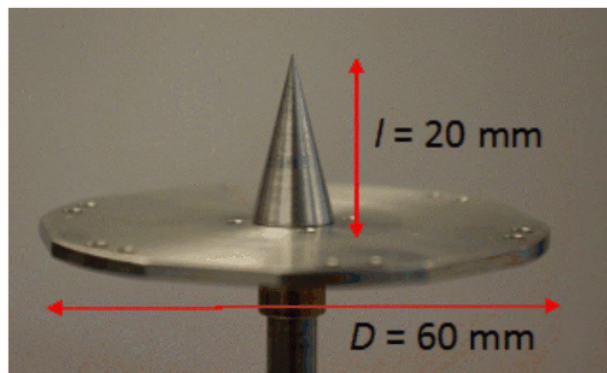

117
118   *Figure 4. The shape of the SEIS foot. The conical spike has a maximum diameter of 10 mm.*

119   2.2. Martian simulant

120   The selection of a relevant Martian regolith simulant is a difficult task (Seiferlin et al. 2008).

121   Given the data provided by the MER, MSL and Phoenix missions and by thermal inertia

122   measurement (see above), it was decided to adopt the Fontainebleau sand (NE34), a well

123   sorted rounded sand with an average grain diameter D_{50} = 220 µm (a little bit larger than

7

124   the 170 µm estimated value at the InSight site) and a uniformity coefficient C_u = 1,57 (the

125   maximum and minimum void ratios are e_{min} = 0.54 and e_{max} = 0.86, respectively, Andria-

126   Ntoanina 2011). The grain size distribution curve and a SEM photo showing the rounded

127   shape of the grains are presented in Figure 5. As observed in Figure 2, it is possible that the

128   InSight regolith be less well sorted with more fine particles, but it is presently difficult to get

129   further precision about the exact in-situ grain size distribution. Observations from previous

130   missions also indicated a loose state of the regolith (Golombek et al. 2008) recently

131   confirmed by local thermal measurements conducted at the surface by the HP^3 mole (Grott

132   et al. 2021).
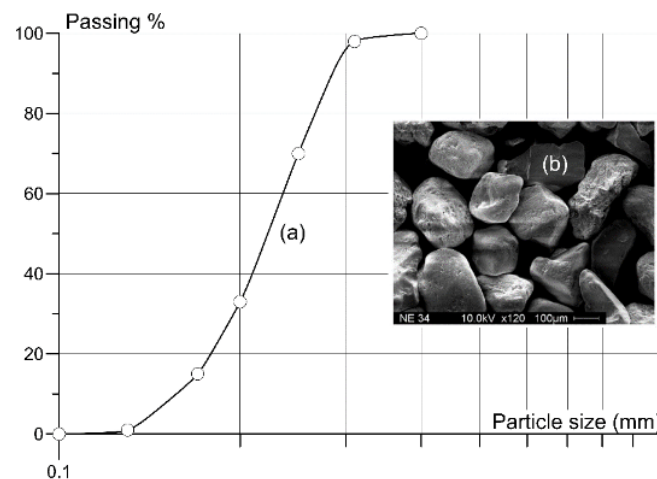
133
134   *Figure 5. NE 34 Fontainebleau sand: a) Grain size distribution; b) Scanning electron microscope*
135   *photo of the showing the subrounded grains (after Andria-Ntoanina 2011).*

136   2.3. Experimental set-up

137   The precision of the experimental device used by Karakostas et al. (2013) was significantly

138   improved by adopting high precision sensors for the measurements of both force and

139   displacement (0.1µm), together with a stiff device designed to support the displacement

8

140   (6x10^{-4} N) transducer and a thermal insulation device of the whole system. The device

141   (Figure 6) consists of a sand container of diameter 240 mm and height 120 mm placed on

142   the plateau of a standard 100 kN triaxial press, allowing for upwards displacement at

143   constant speed at 0.080 mm/min. The diameter of the container was constrained by the

144   space available between the two rods of the triaxial press.
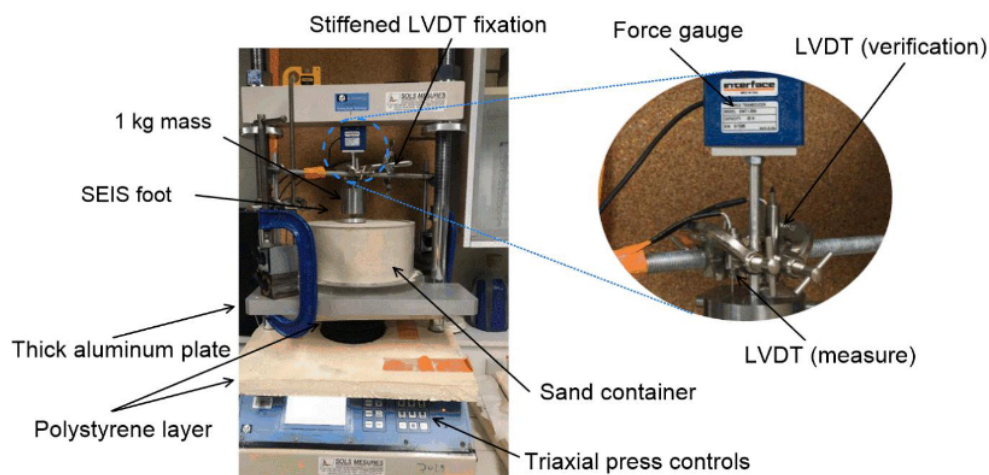
145
146   *Figure 6. Experimental set-up, showing more details the fixation of the mass to the force gauge*
147   *and the LVDTs providing the vertical displacement.*

148   The relevance of the container dimensions with respect to boundary conditions was

149   examined through elastic calculations based on Sneddon (1946)'s solution of a rigid circular

150   plate on a semi-infinite elastic homogeneous space (see Appendix), with the following

151   expression of the vertical displacement Δz:

$$\Delta z = \frac{\pi}{2}(1 - \nu^2)\frac{\sigma_V R}{E} = \frac{F}{2RE}(1 - \nu^2) \tag{1}$$

153   where R is the disk radius, F the applied force, σ_v = F / π R^2 the average applied vertical

154   stress, E the Young modulus and ν the Poisson coefficient. A Young modulus typical of loose

155   sands (E = 20 MPa, Massarsch 2015) was adopted and ν was taken equal to 0.22 (Delage et

9

156   al. 2017). Equation 1 allows analysing stresses on the boundaries of the mould, as shown in

157   Figure 7. This analysis reveals slight changes in stress at the bottom (5% for σ_z and 2% for

158   τ_{zx} of the vertical stress applied on the surface) and at the periphery, leading to a vertical

159   strain ε_z = 0.001% at bottom (compared to 0.018% below the disk).
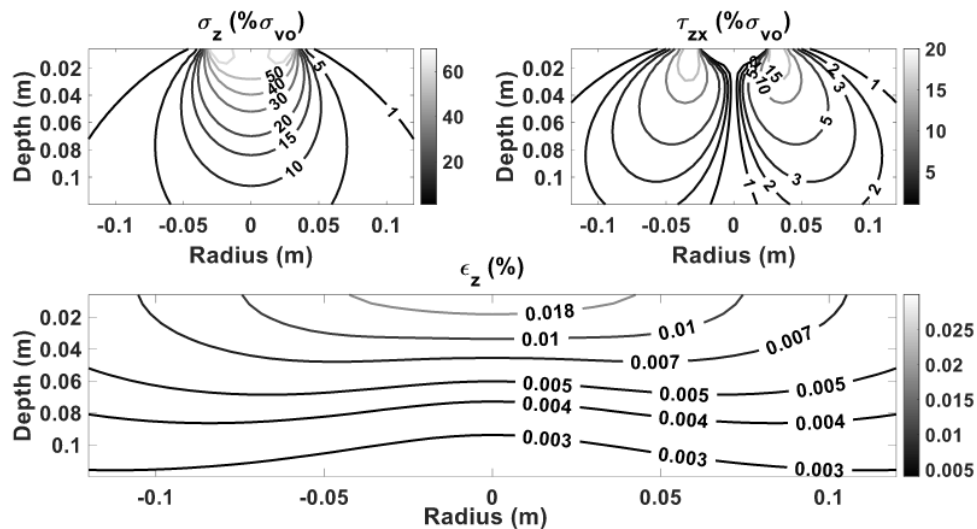
160
161   *Figure 7. Elastic calculations of the vertical and shear stress (presented as percentages of the*
162   *applied vertical stress) and of the vertical strain below the foot under the SEIS weight, based on*
163   *Sneddon (1946)'s elastic solution.*

164   Finite element elastic calculations were also carried out with the Plaxis code to account for

165   possible effects due to the dimensions of the mould. Calculations made with the mould (240

166   mm diameter and 120 mm height) were compared to those with a much larger container

167   comparable to a semi-infinite space (600 mm diameter and 550 mm depth). The differences

168   obtained between the vertical displacements were 5.8 x 10^{-4} µm/N on the lateral boundary

169   and 0.04 µm/N in the middle axis. They were considered small enough to conclude that the

170   semi-infinite hypothesis used in Sneddon's approach was satisfactory for the mould used.

171   Compared to the 220 µm average diameter of the sand grains, the small displacements

10

172   calculated would result in a tiny movement of the grains at the interface with the container,

173   with no significant effect on the disk penetration in the centre.

174   The option adopted in the work was to keep the real (Martian) foot dimensions by reusing

175   the foot model used during the SEIS foot design (Karakostas et al. 2013), by putting it in

176   contact with a simulant with grain size and shape comparable (albeit slightly larger) to those

177   of the InSight regolith, and by loading it up to the force supported by each foot on Mars.

178   The length scale used is 1 (e.g., $L^m/L^p=1$, where L^m is the length of the model and L^p is the

179   prototype's length), leading to a disagreement in the similitude scale for stresses, that can

180   be <mark>analysed</mark> by splitting stresses into those due to the seismometer weight σ_s (with a scale

181   relationship of 1, e.g., $\sigma_s^m/\sigma_s^p = 1$) and those due to the self-weight of the soil σ_g, which is

182   2.64 times greater than on Mars. The match is not perfect along the earlier part of

183   penetration, where the stresses due to soil self-weight predominates. However, once the

184   load grows, the issue with similitude on stresses decreases because the induced stresses

185   beneath the foot dominates over the self-weight stresses.

186   The SEIS foot is fixed at the bottom of a cylindrical mass of 1 kg, corresponding to the load

187   supported by one SEIS foot under Mars' gravity, fixed to the horizontal rigid top beam of

188   the press through a force gauge. The experiment is carried out by putting the spike of the

189   foot in contact with the surface of the sand, prior to activating the upwards movement of

190   the press. This allows for the progressive penetration, at a constant displacement rate, of

191   the foot within the sand mass, until reaching the contact between the disk and the sample

192   surface. The spike penetration is monitored through the displacement rate of the press that

193   has been carefully calibrated. Once the disk contacts the sand, a high accuracy in

      11

194   displacement monitoring is achieved by using a LVDT of 4.5 mm range with 0.1 μm

195   resolution.

196   The force measurement was improved by using a 25 N range force gauge (Interface SMT1-

197   25N). To reduce the noise in displacement measurements, a stiffer fixation system for the

198   LVDT was adopted. As seen in Figure 6, the system is made up of two vertical rods strongly

199   fixed on a thick aluminium plate placed on the plateau of the press along a diameter of the

200   container, and of a horizontal rod strongly fixed to the two vertical ones. The 4.5 mm LVDT

201   was fixed on this system, with its stem in contact with the upper side of the 1 kg mass.

202   Another LVDT with a larger range of 20 mm, seen in Figure 6, has also been used for tilt

203   verification. To the same aim, an insulation system from temperature changes and air

204   movements has been set up, with particular attention paid to thermally insulate the two

205   vertical rods of the triaxial press, because of the possible perturbations due to their thermal

206   expansion/contraction on the displacement measurements. The insulation system

207   consisted of a light prismatic box made up of 5 cm thickness expanded polystyrene and cork

208   layer, placed around the device, as seen in Figure 8a, with a small access made through the

209   box for the control system.

12
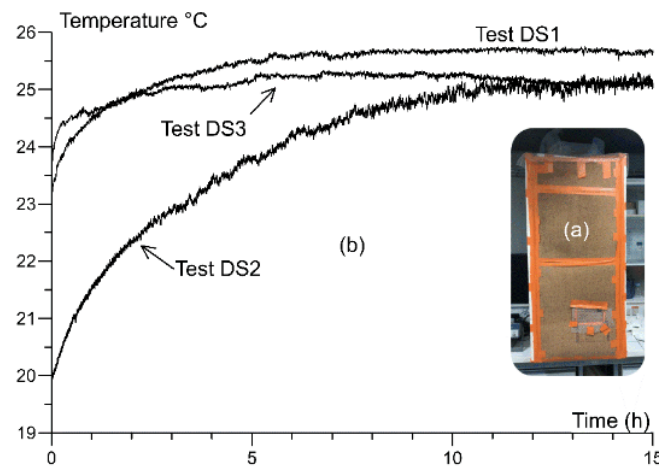
210
211   *Figure 8. a) Thermal insulation of the device; b) temperature stabilisation is reached after 10 hours*
212   *for tests DS1, DS2 and DS3 (see Table 1).*

213   The performance of the insulating system was verified by performing several day/night

214   temperature measurements carried out by means of a thermocouple (able to detect change

215   in temperature smaller than 0.1°C, see Figure 9) inside the box during up to three days. As

216   shown in Figure 8b, thermal stabilization was attained one day after the box was placed

217   around the device. Also, the sand container was insulated from possible thermal

218   perturbations from the press by placing a thick polystyrene plate between the plateau and

219   the thick plate. As observed in Figure 8b and Figure 9, the resulting stabilization after 14

220   hours reduces temperature variations to the order of 0.1°C, which is found quite

221   satisfactory.

13
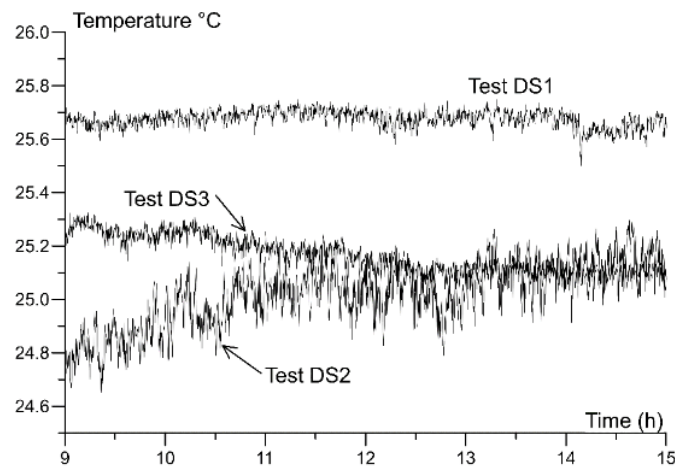
Temperature °C

222
223   *Figure 9. Temperature stabilization in tests DS1, DS2 and DS3 (see Table 1) made possible by the*
224   *thermal insulation of the device, is of the order of 0.1°C.*

225   ### 2.4. Setting-up the low-density simulant specimen

226   Given that the low unit mass of the regolith (1400 kg/m^3 or even less, Golombek et al. 2008,

227   Delage et al. 2017, Morgan et al. 2018, Grott et al. 2021), a dry funnel deposition procedure,

228   already used by various authors (including Tatsuoka et al. 1979, Zlatovic and Ishihara 1997,

229   Lade and Yamamuro 1997, Yamamuro and Wood 2004, Flitti et al. 2019) was adopted. To

230   do so, the sand was gently poured at the centre of a container by using a funnel, keeping a

231   zero falling height between the bottom end of the funnel and the top of the cone. The

232   funnel was gently lifted by hand as the pile rises. An upper Plexiglas ring (8 cm in height)

233   with the same diameter was placed on top of the container. Once the sand pile reached the

234   right height, the ring was removed and the sand in excess was carefully erased to get a

235   smooth horizontal upper plane surface. To minimise any disturbance, the sample was

236   prepared close to the press and to a scale, on a mechanically insulating polystyrene layer.

237   Once prepared, it was very carefully placed (no walking) on the scale for weighing, prior to

238   be placed on the platen of the press. Once on the platen, the erased top surface of the sand

14

239 <mark>was inspected to make sure that it stayed at the top of the container, which was the case.</mark>

240 The unit mass of the deposited sand samples was found to be between 1.403 and

241 1436 kg/m^3 (see Table 1). It corresponds to an average density index I_d = 6 %, indicating a

242 very loose state of the specimen.

243   2.5. Starting the test

244 Once the sample placed on the platen of the press, the thermal insulation box was placed

245 and data acquisition started. As already mentioned, almost one day was necessary to reach

246 temperature stabilization, a mandatory condition for proper displacement measurements.

247 The plateau was moved at a low velocity of 0.08 mm/min to adequately monitor all relevant

248 parameters. Various loading and unloading cycles were applied at different forces to

249 investigate the dependence of the elastic response with respect to stress (see Table 1).

250   3. Experimental results

251 Most preliminary tests were aimed at establishing the validity of the device and at checking

252 repeatability. To do so, it was found simpler to carried out tests with the 60 mm disk of

253 diameter (without spike), because it allowed for an easier detection of the first sand/disk

254 contact. As seen in Table 1, 10 tests were conducted with the disk. Once the performance

255 of the system assessed, it was found that only 3 tests with the foot (disk + spike) were

256 enough. The data obtained are presented in Table 1, including the values of the spring

257 coefficient K_c determined from load cycles under various forces, and K_f from the final

258 unloading and the Young moduli (E_c and E_f). The latter was derived under the hypothesis of

259 elastic semi-infinite homogeneous half-space, as commented later on.

15

260   *Table 1. Experimental program carried out.*

N°	Unit mass kg/m³	Max. p_t* μm (± 0.1)	Max. force N (± 0.01)	Load cycles min – max N (± 0.01)	Slope K_c cycle MN/m (± 0.07)	Slope K_{fu} final unload MN/m (± 0.07)	Young modulus E_c cycle MPa (± 1.1)	Young modulus E_{fu} final unload MPa (± 1.1)
				Disk only				
D1	1421	412.6	10.48	8.14 - 9.63	1.32	1.19	20.89	18.8
D2	1432	534.1	10.39	2.72 - 1.57	0.28	1.47	4.46	23.31
				7.51 - 5.53	1.31		20.76	
D3	1413	419.6	10.47	9.30 - 8.06	1.33	1.09	21.11	17.21
D4	1389	605.9	10.15	4.00 - 2.83	0.37	1.43	5.84	22.68
D5	1421	485.5	10.27	3.01 - 2.07	0.27	1.36	4.23	21.57
				5.67 - 3.32	0.82		12.94	
D6	1436	438.2	10.	9.46 - 7.87	1.23	1.47	19.53	23.31
D7	1423	392.5	10.01	6.92 - 5.62	1.03	0.93	16.38	14.71
D8	1409	605.4	10.97	3.12 - 1.77	0.63	0.76	10.03	11.97
				5.53 - 3.02	1.15		18.17	
D9	1428	348.6	9.80	8.77 - 7.44	1.16	1.53	18.37	24.27
D10	1435	408.3	10.31	8.98 - 6.37	1.47	1.37	23.25	21.73
				Disk + spike				
DS1	1428	607.4	10.6	8.55 6.49	1.11	1.087	17.59	17.24
DS2	1403	598.4	9.91	8.81 - 6.77	1.26	0.825	20.02	13.09
DS3	1418	611.3	10.56	- 7.40	1.18	0.936	18.65	14.85

261   * p_t: penetration

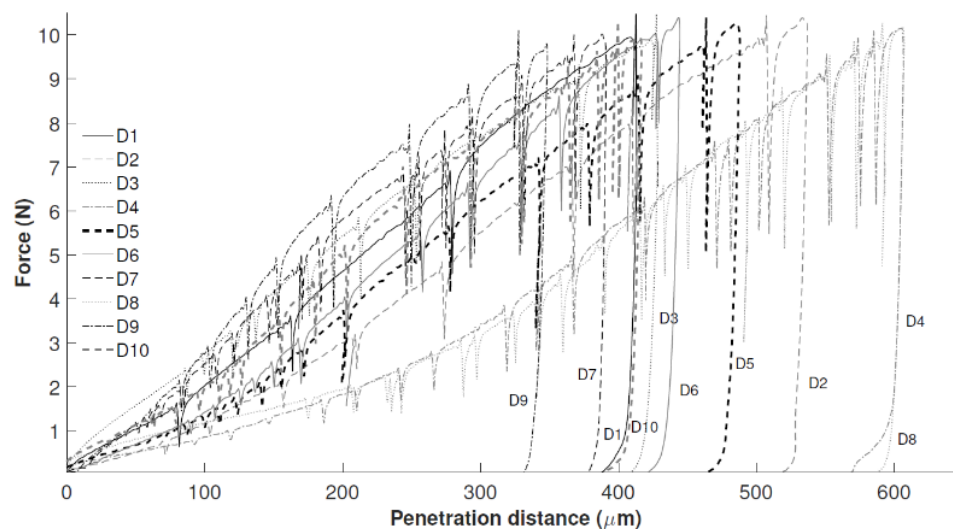## 3.1. Penetration tests with the disc

263   10 tests were carried out with the disk up to a maximum force of 10 N, i.e., the force applied

264   on the ground by each SEIS foot on Mars. Half of them were performed to determine,

265   through a load cycle, the elastic response under 10 N. 5 others were performed under

266   smaller stresses to characterize the variation of the elastic response with stress. All final

267   unloading sequences were also used to determine the K_f coefficients and the E_f Young

268   moduli, as indicated in Table 1.

269   Figure 10 shows the penetration curves of the 10 tests in terms of force (N) with respect to

270   the penetration distance (μm) monitored by the 4.5 mm range LVDT. The Figure shows

16

271   some variability in the maximum penetration observed that ranges between around 400

272   µm for 7 tests and around 600 µm for the other 3. The responses at the beginning of the

273   series of the 7 tests show a stronger increase in force with respect to the displacement. A

274   comparable slope is however reached for the three other tests after a penetration of 300

275   µm.

276
277   *Figure 10. Force-penetration curves for the 10 tests performed with the disc.*

278   All curves show many spikes corresponding to sudden decreases in force, followed by a

279   force recovery along several micrometres that brings back the curve along the initial one

280   that are typical of slip and stick phenomena (Cain et al. 2001).

281   As indicated in Table 1, the elastic response under the SEIS weight (10 N) and thus very small

282   stresses was investigated through cycles in force. Figure 11 shows a cycle performed during

283   test D10 between 8.98 and 6.37 N (force amplitude of 2.61 N), with a resulting penetration

284   response between 395.65 and 397.4 µm (amplitude of 1.75 µm). The curve shows that the

285   decrease in force, resulting from stopping and reversing the direction of the movement of

17

286   the plateau, is not instantaneous, with a progressive decrease in force between 9.67 and

287   9.29 N occurring along 0.8 µm, followed by a frank linear decrease in both force and

288   displacement. A very slight hysteresis is observed, with a difference of 0.2 µm between the

289   two points at 8 N, showing quite a good reversibility and linearity of the response. A value

290   of an elastic spring constant $\Delta F/\Delta d$ of 1.47 x 10^6 N/m is derived from the graph.
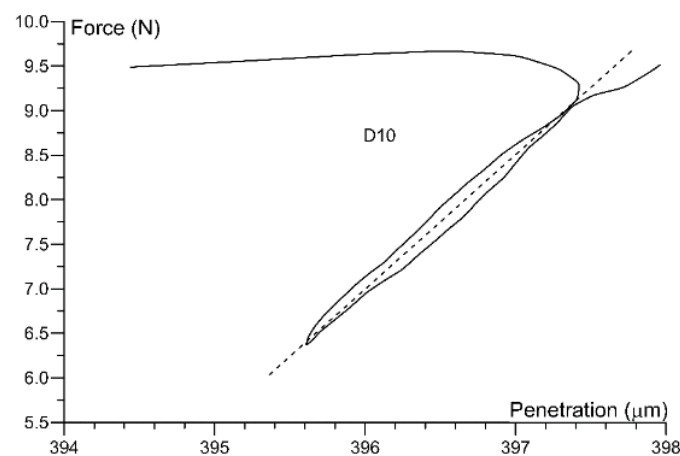

291
292   *Figure 11. Load-unload cycle performed between 8.98 and 6.37 N in test 10 (disk only). The*
293   *stiffness coefficient given by the slope is k = 1.47 x 10^6 N/m.*

3.2. Penetration tests with the foot (disk + spike)

295   The difficulty was to accurately determine the first contact between the spike and the sand,

296   an impossible task if based on force measurement. Since it was easier to detect the contact

297   between the disk and the sand, it was decided to set this point at zero and to plot back the

298   penetration of the spike, as shown in Figure 12a. The curve shows that the penetration of

299   the spike along the first 17 mm (17 000 µm to compare to the 400 − 600 µm of disk

300   penetration) provides no significant added effect of the spike in the loose sand (added

301   contribution between 0.14 and 0.54 N). The Force/Penetration curve of test DS1 is

302   presented in Figure 12 a and b, showing no significant force mobilisation below 3 mm and

18

303   a maximum force of 0.14 N obtained just before the sand/disk contact is reached. The

304   monitored forces also give an idea of the force gauge accuracy that can be estimated ± 0.01

305   N. The sudden drops in force previously observed with the disk and typical of stick and slip

306   are also seen with the cone (at 5 200 and 9 100 µm).
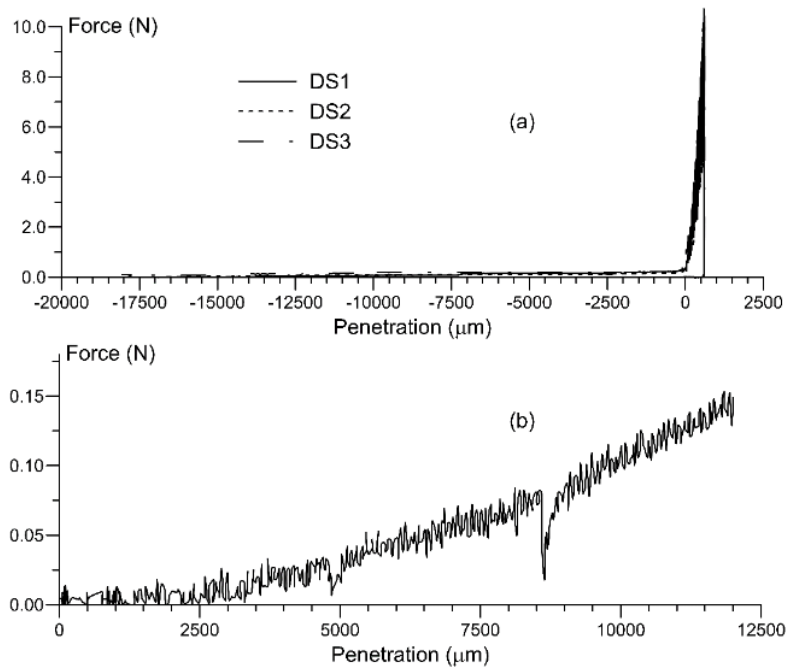
307
308   *Figure 12. a) Force-penetration curves for the 3 tests performed with the foot (disk+spike). Note*
309   *that the force significantly increases once the disk contacts the sand surface. The start of the*
310   *disk/sand contact is taken as 0 for the x-axis, and the curves are started at a point obtained by*
311   *subtracting the length of the spike (- 20 000 µm), b) Detailed force penetration curve of the spike*
312   *alone for test DS1, with a maximum force of 0.14 N reached just before sand/disk contact. Two*
313   *stick-slips are observed at around 4800 and 8600 µm.*

19
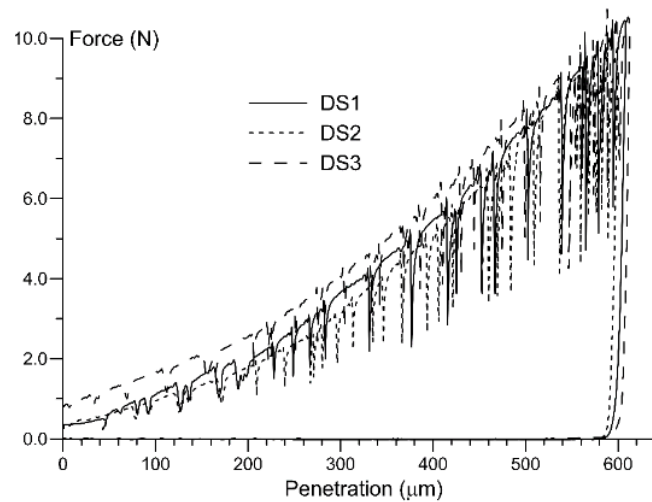
314
315 *Figure 13. Force penetration curves for the 3 tests carried out with the foot (disk + spike) once the*
316 *spike has fully penetrated the sand and the disk is in contact with the sand.*

317　The curves illustrating the interaction between the foot and the sand (Figure 13) are similar

318　to those obtained without the spike, confirming the tiny effect of the spike. A maximum

319　penetration of 600 μm was obtained in these tests, like in three of the tests with the disk

320　only (Figure 10). Reversible load cycles similar to that presented in Figure 11 were also

321　observed, confirming little effect of the spike on the elastic response.

322　4. Interpretations and discussion

323　　4.1.General considerations

324　The challenge of setting up an experimental device able to deal with very low stress and

325　strain has been met, thanks to special care devoted to the thermal insulation and to the

326　stiffness of the device, resulting in a precision of around 0.1 μm in displacements. The

327　maximum disk penetration obtained with our device under the weight of the SEIS (under

328　Mars gravity - around 10 N) is between 400 and 600 μm, whereas the average grain

20

329   diameter of the Fontainebleau sand, 220 µm, is around two to three times smaller. The low

330   stress in the area affected by the disk penetration hence results in quite small plastic strains

331   that correspond to the displacement of a limited number of grains below the sample

332   surface, illustrated by the slope of the curves of Figure 10. The data of Figure 10 and Figure

333   13 show that the force reached at a displacement corresponding to the average grain

334   diameter is between 2 and 7.5 N. This shows that the beginning of the curve is influenced

335   by the roughness of the surface, that is controlled by the arrangement of the grains. Besides

336   possible effects of local changes in density, this may be the explanation for the less

337   pronounced start of the curves reaching 600 µm. Conversely, the reversible load cycles

338   illustrate a small elastic response of $1.3 - 2$ µm in vertical displacement, to be compared to

339   the 220 µm average diameter of the grains, indicating a limited reorganisation of the grain

340   assembly. The elastic response should mainly be governed by the reversible stress

341   release/recompression at grain contacts, following the Hertz-Mindlin contact theory (Hertz

342   1882, Mindlin 1949).

343   When comparing the penetration curves and the close values of the elastic spring constants

344   of the foot and the disk only (Table 1), no significant added effect of the spike was observed,

345   showing that there is space enough in the loose contracting sand to accommodate the thin

346   spike without any added strength. This probably also holds for the InSight regolith, the low

347   density of which has been confirmed by both the development of a pit around the mole at

348   the start of the penetration of the HP[3] instrument (Golombek et al. 2020) and by some in-

349   situ thermal conductivity measurements that provided estimated unit mass values around

350   1200 kg/m^3 (Grott et al. 2021). Some pebbles, like those observed in Figure 2, have also

21

351   been observed in the excavations created by the rockets during landing and in the mole pit.

352   The possibility of not having full penetration of one of the SEIS feet due blocking by a pebble

353   cannot be completely eliminated. However, the thin shape of the spike is optimum in this

354   regard, allowing easier deviation of the spike along a small enough pebble, and full

355   penetration in the loose regolith.

356   ## 4.2. Elastic interpretation of the response

357   Based on the measurements of elastic spring constants K_v presented in Table 1 and on the

358   simplifying assumption of homogeneous linear and isotropic behaviour of the sand, one

359   derived the Young moduli for all the cycles performed (see Table 1) based on the following

360   expression derived from Sneddon's Equation (1):

361
$$E = \frac{k_v(1-\nu^2)}{2R} \tag{2}$$

362   The elastic strain increment corresponding to the force cycle of Figure 11 is equal to 6×10^{-5}

363   ^{5}, showing that the Young moduli are determined at small deformations, not far from the

364   range of those derived from bender element measurements (10^{-5} - 10^{-6}), as done in Delage

365   et al. (2007). The changes in Young modulus with respect to the average vertical stress at

366   surface are presented in Figure 14 (given the negligible effect of the spike, the calculations

367   for the foot have also been made by using Sneddon's solution).

22
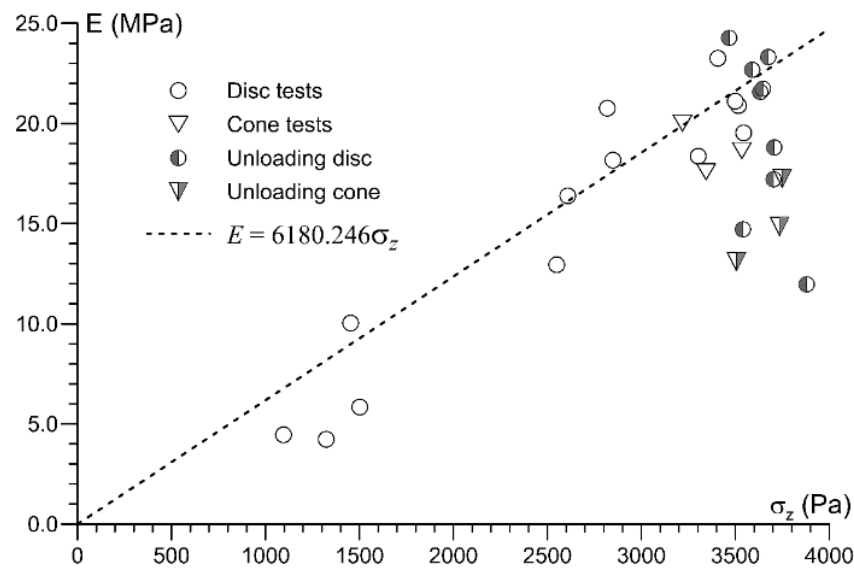
368
369 *Figure 14. Changes in Young modulus with respect to the average vertical stress at surface. Data*
370 *are derived from load cycles tests and from the final unloading step.*

371 In the area corresponding to the SEIS weight (around 3.5 kPa), some dispersion is observed,

372 with E values derived from load cycles between 17.59 and 23.25 MPa. This is an indication

373 of possible changes in local density of the sample at the contact area with the disk/spike,

374 probably enhanced by the small number of grains mobilised by the low applied stress, or

375 for other reasons that are not yet clear, including possible hysteretic material behaviour of

376 the sand. Averaging the values between 3 and 3.5 kPa yields an average E value of 20.07

377 MPa (note that, for some reasons, some of the monotonic unloading coefficients at

378 maximum force stay well below the line, with values as small as 11.97 – 14.85 MPa). Possible

379 effects of changes in Young modulus with depth, suggested by the data of Figure 14, were

380 investigated by carrying out finite elements calculations with a linear change of E with

381 depth, in a model composed of 12 layers of 1 cm thickness. The difference in settlement at

23

382   surface was found equal to 0.0468 μm/m, indicating negligible effects of changes in Young

383   modulus with depth.

384   The linear changes in Young modulus with respect to changes in average vertical stress (a

385   value easy to calculate under a rigid plate) observed in Figure 14 are distinct from the well-

386   known power law that relates the Young modulus with the confining stress, defined by the

387   two following equations (e.g. Santamarina et al. 2001):

388
$$V_p = \alpha \left(\frac{p}{1\,kPa} \right)^{\beta} \tag{3}$$

389   and

390
$$E = \rho V_p{}^2 \left(\frac{3 - \frac{4}{l^2}}{l^2 - 1} \right) \tag{4}$$

391   with $l = \sqrt{\frac{2(1-\nu)}{1-2\nu}}$

392   where p is the mean stress, and α (m/s) and β (-) two fitted parameters. Delage et al. (2017)

393   obtained $\beta = 0.3$ and $\nu = 0.22$ on three different (more angular) Martian simulants. Following

394   Santamarina et al. (2011), it was found more relevant to adopt, for subrounded grains, a

395   slightly smaller value of 0.28, which results in having a power law with $\beta = 0.56$, slightly

396   larger than the 0.5 value commonly adopted for sands (e.g., Hardin and Black 1966,

397   Oztoprak and Bolton 2013). The significant difference with the linear changes observed in

398   Figure 14 is related to the use of average vertical stress σ_z instead of mean stress ((σ_z + 2 σ_x

399   /3, since $\sigma_x = \sigma_y$). Inspection of the Sneddon's expressions of σ_z, σ_x and σ_y (see Appendix)

400   shows that the relation between σ_z and p is far from being simple, with the added difficulty

401   of properly estimating the relevant layer thickness needed to estimate p under the disk.

24

402 Knowing E allows for the calculation of the other parameters governing the SEIS/ground

403 interaction used in Fayon et al. (2019) in their modelling of the SEIS ground interaction, i.e.,

404 the horizontal spring coefficient k_h and the torque C_h (Poulos and Davis 1974):

405

$$k_h = \frac{16\,ER(1-v)}{(7-8v)(1+v)} = 1.17 \times 10^6 N/M \tag{5}$$

406

$$C_h = \frac{4\,ER^3}{3(1-v^2)} = 756.6\,N.m \tag{6}$$

407 Given that the Young modulus has been derived at a strain of 6 x 10^{-5}, another interesting

408 seismic parameter that can be derived is the compression wave velocity at surface,

409 according to the following equation:

410

$$V_p = \sqrt{\frac{E(1-v)}{\rho(1+v)(1-2v)}} \tag{7}$$

411 in which ρ is the regolith unit mass. Adopting E = 20 MPa, ρ = 1.400 kg/m^3 and v = 0.22

412 yields a value of compression wave velocity of 128 m/s, in the expected range for sands

413 under low confinement. Interestingly, this is also in a good agreement with the in-situ

414 velocities at the surface of Mars derived from analysing the seismic signals received by SEIS

415 from HP^3 hammering at around 0.3 m deep, and 1.1 m away, equal to 118 $\pm$ 34 m/s for a

416 surface layer approximately 30 cm thick (Lognonné et al. 2020).

417 However, note that these satisfactory agreements do not necessarily prove that our

418 experiment exactly reproduces the situation on Mars. Some limitations have been discussed

419 above in this regard, both in terms of simulant and scale effects. The calculations here are

420 also made based on a simplifying assumption of an equivalent homogeneous isotropic semi-

25

421 infinite medium, whereas it is known that there is an increase of the elastic modulus of

422 granular media with increased mean stress, as shown in Figure 14. Beside the detailed

423 geological examination of the surface (Golombek et al. 2020), further investigations are

424 presently carried out in this regard within the Near Surface Working Group of the InSight

425 Science Team, based on visual and geological analyses, on the local measurements of

426 thermal inertia, on the seismic signals received by SEIS and on the thermal data provided

427 by HP^3. Based on thermal inertia measurement, a possibility could be to have a finer

428 material with some cohesion, which would also be compatible with the very low density

429 suspected.

5. Conclusions

431 Some improvements were made on the specific device that allowed to design the final

432 shape of the SEIS foot (Lognonné et al. 2019) and to provide the first estimation of the

433 elastic parameters governing the interaction between a Martian simulant and the SEIS foot

434 as analysed in Fayon et al. (2018). To successfully carry out accurate tests in conditions of

435 very low stresses (< 4 kPa) and displacements (< 600 μm), particular care was taken in

436 optimising measurements by using a stiff system to support the container and the LVDT

437 gauges, by using an adapted force gauge and a complete thermal insulation device, allowing

438 to get rid of any perturbation that could result from the thermal expansion/contraction of

439 the loading system, provided a time period of 24h was waited for to ensure a constant

440 temperature with variations smaller than 0.5°C. This high precision device allowed to

441 successfully carry out interaction tests between both a disk and the foot. The tests showed

26

442   that, under the SEIS weight, the maximum penetration in the simulant adopted was around

443   600 μm, i.e., less that the thickness of a layer made up of 3 grains of Fontainebleau sand, a

444   well graded rounded sand with an average grain diameter of 220 μm. As a consequence,

445   the start of the penetration curves was affected by the roughness of the specimen surface,

446   who resulted in having maximum penetration between 400 and 600 μm, i.e., around twice

447   the diameter of a grain. The large number of tests conducted on loose specimens with dry

448   unit mass around 1400 kg/m^3 (density index of 6%) showed reasonable repeatability, with

449   however some dispersion in measured modulus related to possible changes in local density.

450   The elastic response was investigated by conducting stress cycles at various force levels that

451   provided fairly reversible responses with small hysteresis. A simplified analysis considering

452   a homogeneous elastic isotropic semi-infinite medium was carried out to determine the

453   dependency of the Young modulus with respect to the average vertical stress. The linearity

454   observed was distinct to the power law observed with respect to the mean stress, a value

455   difficult to estimate in our case. It was also shown that the effect of the spike in a loose

456   regolith was not significant. The order of magnitude of the Young modulus under the SEIS

457   foot is 20 MPa, a reasonable value for loose sand on the Earth. This value was found

458   compatible with previous laboratory estimations of the surface compression wave velocity

459   and also with in-situ seismic measurements carried out on the InSight landing site by SEIS,

460   from the hammering sessions of HP^3. The data obtained from this improved system will

461   allow for a better determination of the SEIS – regolith interaction and of the resulting

462   resonance frequencies (Fayon et al. 2018). They of course could be improved in the future,

463   once better knowledge about the regolith simulant is obtained. They can also be used for

27

464   the resonance frequencies of the lander itself, that appeared to also have significant effects

465   on the SEIS measurements.

6. Acknowledgements

7. References

477   Andria-Ntoanina, I. (2011). Caractérisation dynamique de sables de référence en

478   laboratoire - Application à la réponse sismique de massifs sableux en centrifugeuse.

479   Thèse Université Paris-Est - Ecole des ponts ParisTech.

480   Arvidson R.E., Guinness E. A., Dale-Bannister M., Adams J., Smith M., Christensen P.R.,

481   Singer N.B. (1989). Nature and Distribution of Surficial Deposits in Chryse Planitia and

482   Vicinity, Mars. Journal of Geophysical Research 94 (b2), 1573-1587.

483   Arvidson, R. E. et al. (2004a). Localization and physical properties experiments conducted

484   by Spirit at Gusev crater. Science 305, 821–824.

485   Arvidson, R. E. et al. (2004b). Localization and physical properties experiments conducted

486   by Opportunity at Meridiani Planum. Science 306, 1730–1733.

28

487   Banerdt W.B., Smrekar S.E., Banfield D., Giardini D., Golombek M., Johnson C.L., Lognonné

488   P., Spiga A, Spohn T. et al. (2020). Initial results from the InSight mission on Mars. Nature

489   Geoscience (13), 183–189.

490   Bates J.R., W.W. Lauderdale, H. Kernaghan (1979). ALSEP Termination Report, NASA

491   Reference Publication Series, NASA-RP-1036, S-480, 914-40-73-01-72, p. 162

492   Cain, R., Page, N., and Biggs, S. (2001). "Microscopic and macroscopic aspects of stick- slip

493   motion in granular shear". *Physical Review E*, Vol 64, No 016413. pp 1-8.

494   Delage, P., Karakostas, F., Dhemaied, A., Belmokhtar, M., Lognonné, P., Golombek, M., De

495   Laure, E., Hurst, K., Dupla, J. C., Kedar, S., Cui, Y. J., & Banerdt, B. (2017). An Investigation

496   of the Mechanical Properties of Some Martian Regolith Simulants with Respect to the

497   Surface Properties at the InSight Mission Landing Site. Space Science Reviews, 211(1–4),

498   191–213. https://doi.org/10.1007/s11214-017-0339-7

499   Fayon, L., Knapmeyer-Endrun, B., Lognonné, P., Bierwirth, M., Kramer, A., Delage, P.,

500   Karakostas, F., et al. (2018). A Numerical Model of the SEIS Leveling System Transfer

501   Matrix and Resonances: Application to SEIS Rotational Seismology and Dynamic Ground

502   Interaction. In Space Science Reviews (Vol. 214, Issue 8). Springer Nature B.V.

503   https://doi.org/10.1007/s11214-018-0555-9

504   Flitti, A., Della, N., De Kock, T., Cnudde, V., & Verástegui-Flores, R. D. (2019). Effect of initial

505   fabric on the undrained response of clean Chlef sand. *European Journal of Environmental*

506   *and Civil Engineering*, 1-16.

507   Goetz, W., Pike, W. T., Hviid, S. F., Madsen, M. B., Morris, R. V., Hecht, M. H., Staufer, U.et

508   al. (2010). Microscopy analysis of soils at the Phoenix landing site, Mars: Classification of

509   soil particles and description of their optical and magnetic properties. Journal of

510   Geophysical Research E: Planets, 115(8), 1–23. https://doi.org/10.1029/2009JE003437.

511   Golombek, M.P., J. A. Grant, L. S. Crumpler, R. Greeley, R. E. Arvidson, J. F. Bell III, C. M.

512   Weitz, R. Sullivan, P. R. Christensen, L. A. Soderblom, and S. W. Squyres (2006a). Erosion

513   rates at the Mars Exploration Rover landing sites and long-term climate change on Mars.

514   J. Geophys. Res., 111, E12S10, doi:10.1029/2006JE002754.

29

515 Golombek, M. P. , L. S. Crumpler, J. A. Grant, R. Greeley, N. A. Cabrol, T. J. Parker, J. W. Rice

516 Jr., J. G. Ward, R. E. Arvidson, J. E. Moersch, et al. (2006b). Geology of the Gusev cratered

517 plains from the Spirit rover transverse. Journal of Geophysical Research, Vol. 111,

518 E02s07, doi:10.1029/2005je002503.

519 Golombek M.P., A.F.C. Haldemann, R.A. Simpson, R.L. Fergason, N.E. Putzig, R.E. Arvidson,

520 J.F. Bell III., M.T. Mellon (2008). Martian surface properties from joint analysis of orbital,

521 Earth-based, and surface observations, in The Martian Surface: Composition, Mineralogy

522 and Physical Properties, ed. by J.F. Bell III. (Cambridge University Press, Cambridge,

523 2008), pp. 468–497. Chap. 21

524 Golombek, M., Warner, N. H., Grant, J. A., Hauber, E., Ansan, V., Weitz, C. M., Williams, N.,

525 Charalambous, C., Wilson, et al. (2020). Geology of the InSight landing site on Mars.

526 Nature Communications, 11(1), 1–11. https://doi.org/10.1038/s41467-020-14679-1

527 Grott M., T. Spohn, J. Knollenberg, C. Krause, T.L. Hudson, S. Piqueux et al. (2021). Thermal

528 Conductivity of the Martian Soil at the InSight Landing site from HP3 Active Heating

529 Experiments. Journal of Geophysical Research - Planets, doi 10.1002/essoar.10506340.1.

530 Hardin, B. O. & Black, W. L. (1966). Sand stiffness under various triaxial stresses. J. Soil Mech.

531 Found. Div. ASCE 92, No. SM2, 667 – 692.

532 Hertz, H. (1882), ''Ueber die Berührung fester elastischer Körper'' (''On the fixed elastic

533 body contact''), Journal für die reine und angewandte Mathematik (Crelle), Vol. 92, pp.

534 156-71.

535 Karakostas F., P. Delage, E. De Laure, A. Dhemaied, J.C. Dupla, A.M. Tang, Y.J. Cui. 2013. The

536 geotechnical properties of some Mars regoliths simulants and their interaction with the

537 SEIS foot. Research report submitted to IPGP.

538 Latham G.V., M. Ewing, F. Press, G. Sutton, J. Dorman, N. Toksoz, R. Wiggins, Y. Nakamura,

539 J. Derr, F. Duennebier, Passive seismic experiment, in *Apollo 11 Preliminary Science*

540 *Report*, NASA, vol. SP-214 (1969), pp. 143–161

541 Latham, G.V., M. Ewing, F. Press, G. Sutton, J. Dorman, Y. Nakamura, N. Toksöz, R. Wiggins,

542 J. Derr, F. Duennebier, Passive seismic experiment. Science **167**, 455–457 (1970).

543 https://doi.org/10.1126/science. 167.3918.455

30

544 Lognonné, P., Banerdt, W. B., Giardini, D., Pike, W. T., Christensen, U., Laudet, P., de

545   Raucourt, S., Zweifel, P., Calcutt, S., Bierwirth, M., Hurst, K. J., Ijpelaan, F., et al. (2019).

546   SEIS: Insight's Seismic Experiment for Internal Structure of Mars. Space Science Reviews

547   (Vol. 215, Issue 1). https://doi.org/10.1007/s11214-018-0574-6

548 Lognonné P., Banerdt W. B., Pike W. T., Giardini D., Christensen U., Garcia R. F., Kawamura

549   T., Kedar S., Knapmeyer-Endrun B., Margerin L., Nimmo 10, Panning M., Tauzin B. et al.

550   (2020). Constraints on the shallow elastic and anelastic structure of Mars from InSight

551   seismic data. Nature Geoscience, https://doi.org/10.1038/s41561-020-0536-y

552 Massarsch, K.R. 2015. Determination of shear modulus of soil from static and seismic

553   penetration testing. Jubilee Volume. Proceedings in honour of Prof. A. Anagnostopoulos,

554   Technical University of Athens. Ed. M. Kavvadas. Athens 2015. Tsotras ISBN: 978-618-

555   5066-30-7, pp. 335 – 352.

556 Mindlin, R. (1949), ''Compliance of elastic bodies in contact'', Transactions of the ASME,

557   Journal of Applied Mechanics, Vol. 16 No. 3, pp. 259-68.

558 Morgan P., M. Grott, B. Knapmeyer-Endrun, M. Golombek, P. Delage, P. Lognonné, S.

559   Piqueux et al. 2018. "A Pre-Landing Assessment of Regolith Properties at the InSight

560   Landing Site." Space Science Reviews. https://doi.org/10.1007/s11214-018-0537-y.

561 Oztoprak S. and Bolton M.D. (2013). Stiffness of sands through a laboratory test database.

562   Géotechnique 63(1), 54 - 70.

563 Poulos H. G. & Davis E.H. (1974). Elastic Solutions for Soil. Series in Soil Engineering, Wiley.

564 Sneddon, I. N. (1946). Boussinesq's problem for a flat-ended cylinder. Mathematical

565   Proceedings of the Cambridge Philosophical Society, 42 (1) 29 – 39, doi

566   10.1017/S0305004100022702

567 Santamarina J.C., Klein K.A., Fam M.A. 2001. *Soils and Waves* (Wiley, New York)

568 Tatsuoka, F., Iwasaki, T., Yoshida, S., Fukushima, S., & Sudo, H. (1979). Shear modulus and

569   damping by drained tests on clean sand specimens reconstituted by various methods.

570   Soils and Foundations, 19(1), 39–54. doi:10.3208/ sandf1972.19.39

571 Lade PV, Yamamuro JA. (1997). Effects of non-plastic fines on static liquefaction of sands.

572   Canadian Geotechnical Journal; 34(6): 918–28

31

573   Vaid, Y. P., Sivathayalan, S., & Stedman, D. (1999). Influence of specimen-reconstituting

574   method on the undrained response of sand. Geotechnical Testing Journal, 22(3), 187–

575   195. doi:10.1520/GTJ11110J

576   Wood, F. M., Yamamuro, J. A., & Lade, P. V. (2008). Effect of depositional method on the

577   undrained response of silty sand. Canadian Geotechnical Journal, 45(11), 1525-1537.

578   Yamamuro, J. A., & Wood, F. M, . (2004). Effect of depositional method on the undrained

579   behavior and microstructure of sand with silt. Soil Dynamics and Earthquake

580   Engineering, 24(9-10), 751-760.

581   Zlatovic, S., & Ishihara, K. (1997). Normalized behavior of very loose non-plastic soils: Effects

582   of fabric. Soils and Foundations, 37(4), 47–56. doi:10.3208/sandf.37.4_47

8. Appendix

The normal and stress fields presented in Figure 7 are based on Sneddon's solution for a cylindrical shaped indenter. The expressions are presented in more detail below.

Sneddon (1946) provided, from an elastic analysis based on Boussinesq's solution, the following expressions for the stress and strain field under a rigid loaded plate:

$$\sigma_z = \frac{3F}{2\pi} \cdot \frac{z^3}{R^5} \tag{8}$$

$$\sigma_x = \frac{3F}{2\pi} \cdot \frac{x^2 z}{R^5} - \frac{m-2}{3m}\left[-\frac{1}{R\cdot(R+z)} + \frac{(2R+z)x^2}{(R+z)^2 R^3} + \frac{z}{R^3}\right] \tag{9}$$

$$\sigma_y = \frac{3F}{2\pi} \cdot \frac{y^2 z}{R^5} - \frac{m-2}{3m}\left[-\frac{1}{R\cdot(R+z)} + \frac{(2R+z)y^2}{(R+z)^2 R^3} + \frac{z}{R^3}\right] \tag{10}$$

$$\tau_{xy} = \frac{3F}{2\pi} \cdot \frac{xyz}{R^5} - \frac{m-2}{3m}\left[\frac{(2R+z)xy}{(R+z)^2\cdot R^3}\right] \tag{11}$$

$$\tau_{xz} = \frac{3F}{2\pi} \cdot \frac{xz^2}{R^5} \tag{12}$$

32

$$\epsilon_z = \sigma_z / E \tag{13}$$

$$p_t = \frac{1+\nu}{2\pi E} \cdot \left[\frac{z^2}{R^3} - \frac{(1-2\nu)x}{R} \right] \cdot F \tag{14}$$

in which *F* is the force applied on the disk, *z* the depth, x and y the horizontal distance

from the axis, $R = \sqrt{x^2 + y^2 + z^2}$, p_t the penetration and *m* = 1/*v*.

33